International Journal on Magnetic Particle Imaging
Vol 6, No 1, Article ID 2003004, 11 Pages

Infinite Science Publishing

Research Article

Investigating Spatial Resolution, Field Sequences and Image Reconstruction Strategies using Hybrid Phantoms in MPI

Anselm von Gladiss[a,*] · Matthias Graeser[b,c] · Aileen Cordes[a] · Anna C. Bakenecker[a] · André Behrends[a] · Xin Chen[a] · Thorsten M. Buzug[a]

[a] Institute of Medical Engineering, University of Lübeck, Lübeck, Germany
[b] Section for Biomedical Imaging, University Medical Center Hamburg-Eppendorf, Hamburg, Germany
[c] Institute for Biomedical Imaging, Hamburg University of Technology, Hamburg, Germany
[*] Corresponding author, email: {gladiss,buzug}@imt.uni-luebeck.de

Received 7 July 2019; Accepted 26 March 2020; Published online 30 March 2020

Abstract

Hybrid phantoms allow for measurement-based evaluation of particle samples, reconstruction algorithms and field sequences without need of a Magnetic Particle Imaging (MPI) scanning device. Even dynamic hybrid phantoms can be generated using dynamic magnetic offset fields. Multi-dimensional Magnetic Particle Spectrometers are capable of emulating both hybrid system matrices and hybrid phantoms, which can be reconstructed into images. It is shown that a spatial resolution of few hundred micrometres can be achieved for both one- and multi-dimensional excitation using MPI technology. The spatial resolution of reconstructed images increases when including additional receive channels into the reconstruction process. For multi-dimensional imaging the sine-based Lissajous trajectory outperforms the cosine-based Lissajous trajectory in terms of spatial resolution. Both the high signal to noise ratio of a spectrometer and the versatility of hybrid phantom design will enforce innovative measurement-based research on key parameters for MPI.

I. Introduction

It has been previously shown that multi-dimensional Magnetic Particle Spectrometers (MPS) can generate the same magnetic excitation fields as a Magnetic Particle Imaging (MPI) scanning device [1, 2]. When superposing magnetic offset fields in an MPS, hybrid system matrices can be measured. In an MPS, the distance from the sample to the receive coils is very small. Thus, the signal to noise ratio (SNR) is usually higher in an MPS than in MPI devices and measurement results are profiting of a superior SNR. Furthermore, the measurement time of a hybrid system matrix is lower compared to a conventional system matrix measured in an MPI device, as the movement of the particle sample is obsolete.

Phantom data that have been measured in MPI scanning devices were reconstructed successfully using hybrid system matrices [2]. The reconstructed images profit from the superior SNR of a hybrid system matrix but are limited by the SNR of the phantom measurements. As the spatial resolution depends on the SNR, it is limited in the reconstructed images [3]. In this work, hybrid phantoms featuring high SNR are reconstructed into images of high spatial resolution.

When synthesizing new types of particles, improving image reconstruction algorithms, modifying field se-

quences and developing new hardware components for an MPI scanning device, these development steps need to be tested regarding their influence on e.g. the sensitivity and spatial resolution in reconstructed images. Phantom measurements are performed in MPI scanning devices and reconstructed into images. As both the spatial resolution and sensitivity rely on the SNR of an MPI scanning device, research results may vary when being carried out on different devices.

In contrast to measurement-based experiments, field sequences and reconstruction algorithms have been researched using simulation studies [4, 5]. However, as the formulation of a multi-dimensional particle model remains difficult, these results are usually bound to the simplified Langevin-model of the particles which leads to imprecise results [5–7]. Therefore, this work introduces hybrid phantoms for researching MPI key parameters. Measurement data of an MPS provides the particle signal without the need of an MPI scanning device.

The requirements on phantom design for MPI measurements are demanding. The phantom material should be consistent and impermeable, as the particles must not diffuse into the phantom material and the solute must not evaporate. However, the material should be versatile for allowing the design of complex phantoms such as vessel and nested structures. It must not be ferromagnetic for not causing artefacts in image reconstruction. For proving spatial resolution in sub-millimetre range, consistent dividing walls of thickness in micrometre range must be manufactured.

Custom nanoparticles are often synthesised in small batches first, limiting the amount of particles available. When handling large volume phantoms, an appropriate amount of particles needs to be available, as a low concentration of particles results in low SNR.

For measuring very small differences in tracer concentration in different cavities of a phantom, the particles have to be diluted precisely, which is a complex and difficult work. A dilution error may not be comprehended later but only identified by repeating the whole experiment.

The hybrid measurement of phantoms uncouples the measured particle signal from the SNR of an MPI scanning device, the phantom design and the tracer concentration.

In MPI, a measured voltage $u(t)$ is induced by a magnetisation change. Ideally, only the particles inside the field of view (FOV) change their magnetisation. That means, the magnetisation change is spatially limited to the volume of the phantom inside the FOV. Therefore, the signal equation of MPI can be described as

$$\begin{aligned} u(t) &\sim \int_{\Omega} \frac{\partial}{\partial t} M(r,t) d^3 r \\ &= \int_{\Omega} \frac{\partial}{\partial t} c(r) \bar{m}(\|B(r,t)\|_2) e_B d^3 r \\ &= \int_{\Omega_P} \frac{\partial}{\partial t} c(r) \bar{m}(\|B(r,t)\|_2) e_B d^3 r \\ &\approx \sum_{i=0}^{N-1} \frac{\partial}{\partial t} c(r_i) \bar{m}(\|B(r_i,t)\|_2) e_B, \\ \Omega &= \{r \in \mathbb{R}^3\}, \Omega_P = \{r \in \mathbb{R}^3 \mid c(r) \neq 0\} \end{aligned} \tag{1}$$

with the magnetisation M, the magnetic moment $\bar{m}$, the magnetic field B, the spatial particle distribution $c(r)$ and Ω_P being the volume of the phantom. The phantom itself can be discretised into N components and the magnetisation change of these N components may be measured sequentially, provided that the particles do not interact between the single components. The sum over the N measured voltages $u_i(t)$ corresponds to the voltage $u(t)$ which would be measured for the whole phantom

$$\begin{aligned} u(t) &= \sum_{i=0}^{N-1} u_i(t) \\ &\sim \sum_{i=0}^{N-1} \frac{\partial}{\partial t} c(r_i) \bar{m}(\|B(r_i,t)\|_2) e_B \,. \end{aligned} \tag{2}$$

The discrete formulation in (1) and (2) is used for measuring hybrid phantoms. A software phantom is generated and discretised. The discrete components of the phantom can be measured sequentially inside a multi-dimensional MPS as it may emulate an infinitesimal volume of an MPI scanning device. The sum of the measured voltages (see (2)) emulates a phantom measurement inside an MPI scanning device.

As an MPS does not feature a FOV, the spatial dimensions of a simulated phantom are translated into magnetic offset fields. The spatial position and the magnetic offset field B_0 are linked by the magnetic gradient field strength G of an MPI scanning device [8], e.g.

$$x = \mathrm{B}_{0,x} / \mathrm{G}_x \tag{3}$$

for the x-direction.

In [9], the spatial resolution of nanoparticles has been investigated using MPS data. Simulated noise has been added to the measurement results for approximating the detection limit of an MPI scanning device. Both hybrid system matrices and phantoms of different particle samples have been measured in [10]. The spatial resolution in the reconstructed images has been compared to results obtained by an MPI scanning device. The influence of coupling between sending coils of an MPI scanning

device on the signal trajectory and the reconstructed images has been researched using hybrid data [11].

In this work, distinct experiments using both static and dynamic hybrid phantoms are carried out to demonstrate their benefits. The spatial resolution is investigated which can be reached using one-dimensional and multi-dimensional excitation when reconstructing hybrid phantoms with hybrid system matrices. It is examined whether the image quality of reconstructed images profits from including the induced signal of orthogonal receiving coils. Furthermore, the influence of phase variation in the multi-dimensional Lissajous trajectory on the spatial resolution is investigated. It is shown that dynamic phantoms can be emulated. The temporal resolution of reconstructed images is increased by splitting the receive signals.

I.I. 1D excitation

One-dimensional excitation fields are used for particle analysis in MPS and for cartesian trajectories in MPI scanning devices. Here, the spatial resolution of reconstructed images using 1D excitation is examined when acquiring both hybrid system matrices and hybrid phantoms. A hybrid 1D system matrix and a hybrid 1D resolution phantom are measured in a multi-dimensional MPS. Usually, only the receiving signal that is acquired parallel to the excitation direction is used. It has been suggested in [1, 12] that image quality may benefit from using the receiving signal orthogonal to the excitation direction, too. In this work, the receiving signals both parallel and orthogonal to the excitation direction are included into the image reconstruction process.

I.II. 2D excitation

The multi-dimensional Lissajous trajectory is used in MPI scanning devices for moving a field-free point (FFP) over the FOV. It provides a good compromise of temporal and spatial resolution and technical effort [4]. In order to form a Lissajous trajectory, orthogonal sinusoidal signals are superposed. The phase of the sines determines the spatial sampling density, see Figure 1 [13]. The highest sampling density can be reached using a phase of $\phi = 0°$. The drawn lines move closer with increasing phase. At $\phi = 90°$ half the sampling density is reached. The trajectory turns after half its period and samples the same spatial positions again. The influence of this phase variation on the spatial resolution of reconstructed images is being investigated in this work for 2D excitation.

Spiral phantoms have been presented in [14] for comparing measurements in different MPI scanning devices. Here, these spiral phantoms are emulated and the spatial resolution of the reconstructed images is evaluated.

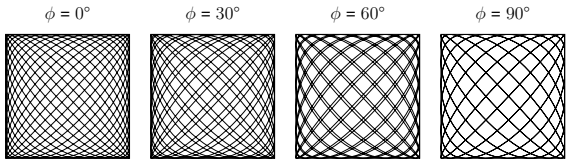

Figure 1: Two-dimensional Lissajous trajectories with different phases ϕ. The phases of both the orthogonal excitation signals $\sin(2\pi f_i t + \phi)$ featuring different frequencies f_i is varied $\phi = [0°, 30°, 60°, 90°]$. For $\phi = 0°$, the Lissajous trajectory has a high and nearly equidistant spatial sampling density in its centre. The higher the phase shift, the more heterogeneously becomes the sampling density. With a shift of $\phi = 90°$, the sampling density is nearly equidistant again in its centre, but only half of the spatial domain is covered in comparison to $\phi = 0°$. A phase shift of $\phi = 90°$ is equivalent to cosine signals. As cosine is an even function, the Lissajous trajectory turns after half its period and samples the same spatial positions again.

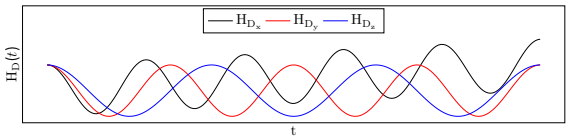

Figure 2: Scheme of a magnetic field sequence for an emulated dynamic hybrid phantom. A 3D drive field excites the particle sample using a Lissajous trajectory with $\phi = 90°$. A ramp is superposed on H_{D_x} with an amplitude of the drive field strength, resembling a movement of the particle sample to the border of the FOV within one drive field cycle.

I.III. Dynamic phantoms

Static phantoms have been emulated using 1D and 2D excitation. They are valuable tools for investigating field sequences and system parameters such as SNR. However, in preclinical and clinical research the measurement of dynamic processes is important in cases such as the change of spatial particle distribution due to blood circulation, or the transport of particles within cells [15, 16]. Therefore, dynamic phantoms are in focus of research [17–19].

Here, in order to emulate motion in space or magnetic field, respectively, a dynamic offset field is superposed to a 3D drive field (see Figure 2) to generate dynamic hybrid phantoms. Furthermore, the temporal resolution of a dynamic measurement is increased by splitting the receive signals of both the measurement and the corresponding system matrix as it has been introduced in [20]. Then, motion artefacts can be reduced and fast dynamic processes can be resolved.

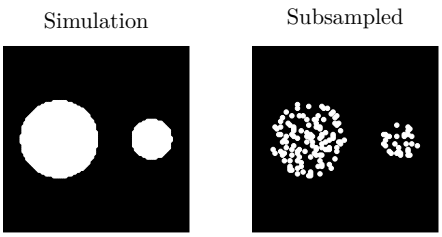

Figure 3: A phantom featuring two circles of different size is simulated on a fine grid of 100 × 100 pixels (left). The two circles consist of 1238 and 310 pixels, respectively. Thus, a hybrid measurement of this phantom would need 1548 single measurements. In order to reduce the measurement time, each circle is undersampled randomly by 10 % (right). Then, only 155 single measurements have to be carried out, which is 124 and 31 measurements for the left and right circle, respectively. A random particle distribution is generated in each circle while keeping both the fine grid of 100 × 100 pixels and a constant particle concentration between the circles.

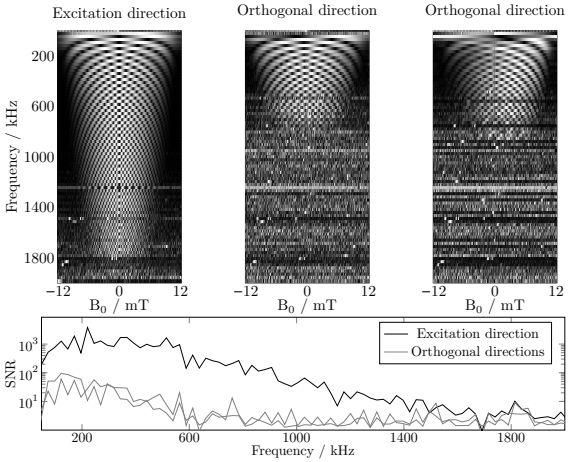

Figure 4: Hybrid 1D system matrix using 1D excitation and SNR of the system matrix measurement. Structures up to 1.8 MHz can be identified in the system matrix of the receive channel parallel to the excitation direction (top left). The structures in higher frequency components are lost in noise. The system matrices of the orthogonal receive channels (top centre and right) show structures up to 700 kHz. The SNR (bottom) corresponds to the visual impression.

II. Materials and Methods

II.I. 1D excitation

A 1D hybrid system matrix has been acquired in a multi-dimensional MPS [21] using an excitation frequency of 24.510 kHz and an amplitude of 12 mT. The magnetic offset field has been varied using a step width of 0.25 mT in the range of [−12 mT, 12 mT]. The receiving signal has been averaged 16,000 times resulting in a measurement time of 0.65 s per position. As particle sample, 30 µl of perimag (micromod Partikeltechnologie GmbH, Rostock) with a particle concentration of 12.5 mg µl^{-1} have been used.

10 hybrid two-dot phantoms have been emulated using the same particle sample, number of averages and excitation field parameters. The two dots have a distance of 0.6 mT and are centred around the magnetic offset field positions [±1 mT, ±3 mT, ±5 mT, ±7 mT, ±9 mT].

The hybrid phantoms are reconstructed using the hybrid system matrix and an unregularised Kaczmarz algorithm with 500 iterations. For reconstruction, frequency components between 65 kHz and 2 MHz featuring a minimum SNR value of 10 are selected. The phantoms are reconstructed first using the parallel receive channel solely and second using all the available receive channels.

II.II. 2D excitation

II.II.1. System matrix

A hybrid 2D system matrix has been measured with excitation field frequencies of 24.509 kHz and 26.042 kHz, field amplitudes of 12 mT and phases of $\phi = 0°$ (see Figure 1). The magnetic offset fields have been varied in the range of [−12 mT, 12 mT] in both x- and y-direction with a step width of 0.5 mT resulting in a system matrix of 49 × 49 pixels. The receive signal has been averaged 50 times. The same particle sample as in Section II.I has been used.

A second hybrid system matrix has been acquired using the same parameters, but with a phase of $\phi = 90°$.

II.II.2. Resolution phantom

A 2D resolution phantom has been simulated on a grid of 512 × 512 pixels. It consists of four different point cloud grids with 2 × 2, 3 × 3, 4 × 4 and 6 × 6 point clouds in the single quadrants. The point clouds are of different size and have a distance of [3 mT, 2 mT, 1.5 mT, 1 mT] to each other (surface to surface). In total, the phantom has magnetic offset field dimensions in the range of [−12 mT, 12 mT].

A very fine grid has been chosen for simulation guaranteeing a round shape of the point clouds. For the hybrid measurement, the discrete points inside each point cloud are subsampled randomly generating a random distribution of particles inside each point cloud while maintaining a constant concentration. A uniform pseudorandom number generator is used for the random subsampling. Figure 3 shows an example for simulating a phantom on a fine grid and then subsampling it to 10 % of the points for a hybrid measurement in order to reduce the measurement time. In this experiment, 5 % of the discrete points inside each point cloud are selected for the measurement.

The measurement parameters and the particle sample have been the same as for measuring the hybrid system matrix. Also, the hybrid phantom is measured twice

using a varied phase ϕ of the Lissajous trajectory.

The measured voltage signals are summed up for each phantom measurement according to (2).

The hybrid phantoms have been reconstructed using an unregularised Kaczmarz algorithm featuring 50 iterations. Frequency components between 50 kHz and 1.2 MHz with a minimum SNR value of 100 have been selected for reconstruction.

II.II.3. Spiral phantoms

Two spiral phantoms with an exponentially increasing flexion have been presented in [14] (see Figure 7 top). One of the phantoms features a channel diameter of 2 mm and distances of 0.36 mm to 6 mm between the spiral curls. The channel diameter of the other phantom is 1 mm.

Both phantoms have been simulated on a fine 2D grid. The spatial dimensions have been translated into magnetic offset fields assuming a magnetic field gradient of 1.25 T m^{-1} in both directions. 2 % and 3 % of the points representing the spirals have been selected for the hybrid measuring, which are about 5000 points for each phantom (see Figure 3).

The acquisition parameters and particle sample have been the same as for the hybrid system matrix. The received voltage signals are accumulated (see (2)).

The spiral phantoms have been reconstructed using a Kaczmarz algorithm featuring 10 iterations and a Tikhonov regularisation factor of $2 \cdot 10^{-7}$. Frequency components between 65 kHz and 1.2 MHz with an SNR value > 5 have been selected for reconstruction.

II.III. Dynamic phantoms

II.III.1. System matrix

A hybrid 3D system matrix has been measured with excitation field frequencies of 24.509 kHz, 26.042 kHz and 25.252 kHz field amplitudes of 12 mT and using cosine excitation ($\phi = 90°$). The magnetic offset fields have been varied in the range of $[-12\,\text{mT}, 12\,\text{mT}]$ in x-, y- and z-direction with a step width of 1 mT resulting in a system matrix of $25 \times 25 \times 25$ pixels.

II.III.2. Phantom

A particle sample has been measured using the same magnetic field sequence first without applying a magnetic offset field. In a reconstructed image, the particle sample would be represented by a dot in the centre of the FOV. Then, motion has been emulated by superposing a magnetic field ramp to the drive field in x-direction from 0 mT to 6 mT and 12 mT within one drive field cycle, respectively (see Figure 2). These ramps correspond to a movement of the particle from the centre of the FOV to halfway and fully to the border of the FOV.

II.III.3. Increasing temporal resolution

Both the system matrix and measurement are acquired in time domain. After correcting them for the transfer function of the receive chain, they are split after half the period T of the exciting field. For a system matrix $\mathbf{S}$ in spectral domain this is

$$\begin{aligned} \mathbf{S}_1 &= \mathscr{F}\{\mathscr{F}^{-1}\{\mathbf{S}\}_{t=[0,T/2)}\} \\ \mathbf{S}_2 &= \mathscr{F}\{\mathscr{F}^{-1}\{\mathbf{S}\}_{t=[T/2,T)}\} \end{aligned} \tag{4}$$

with $\mathscr{F}$ and $\mathscr{F}^{-1}$ being the Fourier and inverse Fourier transform, respectively. Then, two system matrices $\mathbf{S}_1$ and $\mathbf{S}_2$ are obtained representing the first and second halves of the drive field cycle. A corresponding operation is performed on the measurement data. Two image reconstruction problems are then formulated $\mathbf{S}_1 \cdot \mathbf{c}_1 = \mathbf{u}_1$ and $\mathbf{S}_2 \cdot \mathbf{c}_2 = \mathbf{u}_2$ with $\mathbf{c}_1$ and $\mathbf{c}_2$ being the reconstructed particle distributions within the first and second half of the drive field cycle. A drive field phase of $\phi = 90°$ has been chosen as the trajectory pathway is the same for the first and second half of the drive field cycle (see Figure 1).

The static and dynamic phantoms have been reconstructed using a Kaczmarz algorithm featuring 1 iteration and a Tikhonov regularisation factor of 0.1. Frequency components between 60 kHz and 500 kHz have been selected for reconstruction.

The centres of mass have been calculated for the reconstructed images by

$$\mathbf{r}^{\text{CoM}} = \frac{\sum_i I(\mathbf{r}_i) \cdot \mathbf{r}_i}{\sum_i I(\mathbf{r}_i)} \tag{5}$$

with $\mathbf{r}^{\text{CoM}} = \{\mathbf{r}_x^{\text{CoM}}, \mathbf{r}_y^{\text{CoM}}, \mathbf{r}_z^{\text{CoM}}\}$ the centre of mass in x-, y- and z-direction, $\mathbf{r}_i$ a spatial position (a voxel) and $I(\mathbf{r}_i)$ the grey value at position $\mathbf{r}_i$.

III. Results

III.I. 1D excitation

The acquired hybrid system matrices both parallel and orthogonal to the excitation direction are shown in Figure 4. The absolute values of each frequency components have been normalised for visualisation. According to the SNR plots shown in Figure 4, the system matrices of the orthogonal receive channels feature frequency components with SNR values > 10 up to 600 kHz.

The reconstruction results of the 10 two-dot phantoms are visualised in Figure 5 as both grey-value images and intensity plots. When using the receive channel parallel to the excitation direction solely, strong reconstruction artefacts are visible, especially at the edges of the FOV. Using a full width half maximum (FWHM) criterion and a small value threshold, the dots of 7 phantoms can be separated.

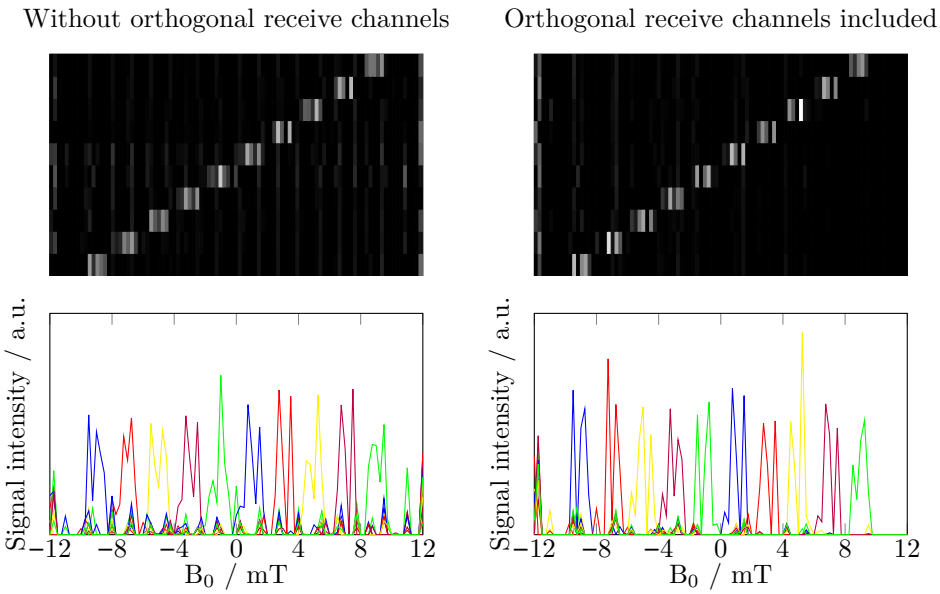

Figure 5: Reconstructed images (top) and intensity plots (bottom) of hybrid 1D resolution phantoms. Two dots with a distance of 0.6 mT to each other have been moved through the FOV with a step width of 2 mT. The hybrid system matrix has a magnetic field resolution of 0.25 mT. For reconstruction, the induced voltage signal of the receive channel parallel to the excitation direction solely (left) and also orthogonal to the excitation direction (right) have been used. When including the orthogonal receive channels, all but one phantoms can be separated using an FWHM approach. Only 7 phantoms can be resolved using the parallel channel solely. A magnetic field resolution of 0.6 mT corresponds to a spatial resolution of 240 µm assuming a magnetic gradient field strength of 2.5 T m^{-1} in an MPI scanning device.

After including the orthogonal receive channels into the reconstruction process, the artefacts are reduced and the SNR of the reconstructed images increases. However, strong artefacts are remaining at the left side of the FOV. Now, 9 phantoms can be separated using the FWHM approach.

When lowering the number of iterations of the Kaczmarz algorithm or when including frequency components of lower SNR, the number of separable phantoms is higher when including orthogonal receive channels.

III.II. 2D excitation

In Figure 6 the reconstruction results of the hybrid 2D resolution phantom are shown. The point clouds with distances of [3 mT, 2 mT, 1.5 mT] are well resolved for both sinusoidal and cosinusoidal Lissajous sampling. Featuring distances of 1.5 mT, the point clouds can be separated visually better using sinusoidal sampling. Near the edges of the FOV, the point clouds are partly distorted or even missing (bottom right).

The point clouds with the nearest distance of 1 mT to each other cannot be resolved reliably. However, a hybrid phantom that consists of this point cloud grid solely can be reconstructed using different reconstruction parameters (Figure 6 bottom). Here, an unregularised Kaczmarz algorithm with 200 iterations has been used together with an SNR-threshold of 50. Intensity plots of the third point cloud row and column are shown. The point clouds are distincted sharper using the sine-based Lissajous trajectory. Furthermore, the point clouds are resolved better along the x-direction (top to bottom).

III.II.1. Spiral phantoms

The reconstruction results of the emulated spiral phantoms are shown in Figure 7 (bottom). The reconstructed spirals match the simulated data. The curls of the spiral are well resolved up to about 1 mT corresponding to a spatial resolution of 800 µm assuming a gradient field strength of 1.25 T m^{-1}.

III.III. Dynamic phantoms

Figure 8 shows reconstructed images of the dynamic phantom and an emulated motion of 12 mT in x-direction within one drive field cycle. The zero plains of xy ($z = 0$) and yz ($x = 0$) are displayed. When using the system matrix for the whole drive field cycle $\mathbf{S}$, the dynamic hybrid phantom is reconstructed as a streak all over its pathway. The phantom can be identified weakly in the yz-plain. Reconstructing with the system matrix representing the first half of the drive field cycle $\mathbf{S}_1$, the phantom is displayed near the centre of the FOV. Using $\mathbf{S}_2$, the phantom is reconstructed near the edge of the FOV. In the yz-plain ($x = 0$), the phantom can only be identified reconstructing with $\mathbf{S}_1$.

10.18416/ijmpi.2020.2003004

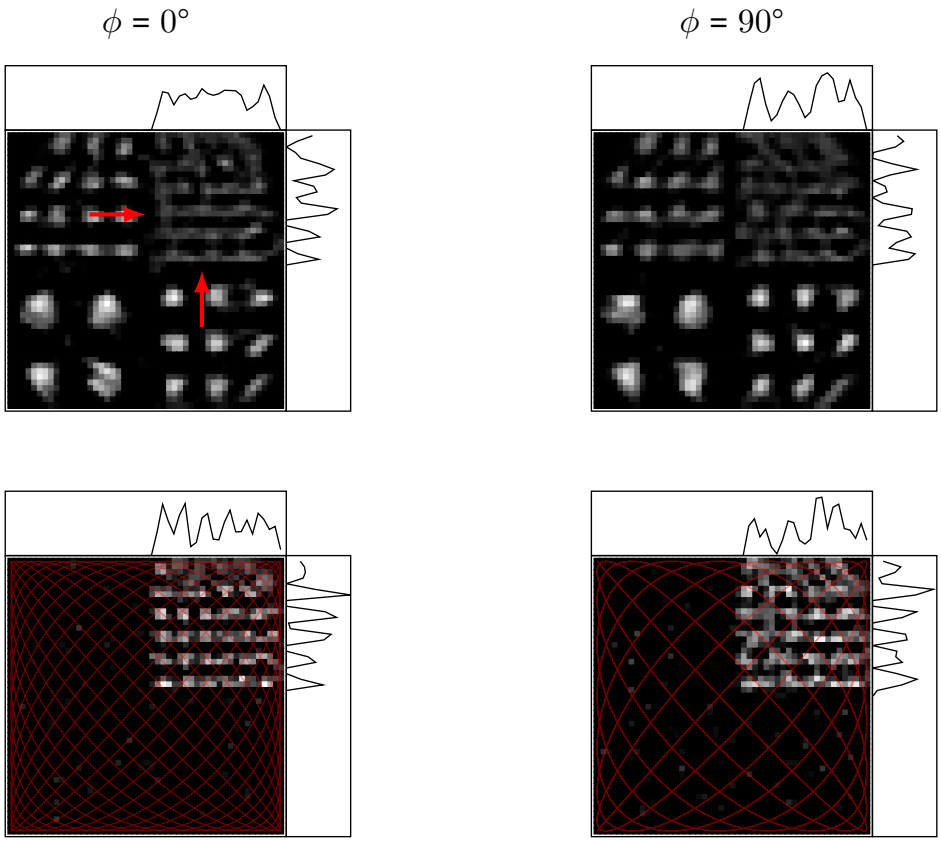

Figure 6: Reconstructed images of hybrid resolution phantoms which have been sampled using a sine-based (left) and cosine-based (right) Lissajous trajectory. The same reconstruction parameters have been selected for both datasets. The spatial resolution in the images is very similar when reconstructing the whole resolution phantom (top). The point clouds with distances of [3 mT, 2 mT, 1.5 mT] to each other are well resolved. There are reconstruction artefacts at the edges of the FOV. When reconstructing the point clouds with a distance of 1 mT to each other solely (bottom), a higher spatial resolution is reached using the sine-based Lissajous trajectory (left). The intensity plot along the third point cloud row and column (see red arrows) confirms the visual impression. The Lissajous trajectories are shown in red visualising the different sampling patterns.

The centres of mass of the reconstructed images have been calculated using a value threshold of 20 %. The static hybrid phantom is reconstructed to the centre of the FOV for each system matrix, which corresponds to the calculated centres of mass. In case of motion to 6 mT in x-direction, the centre of mass is calculated to $r_x = 2.7\,\text{mT}$ for the conventional hybrid system matrix $\mathbf{S}$, which is almost half of the pathway. Using the system matrices representing the first and second half of the drive field cycle, the centres of mass $r_{1,x}^{\text{CoM}} = 2.1\,\text{mT}$ and $r_{2,x}^{\text{CoM}} = 3.6\,\text{mT}$ are calculated to approximately one third and two thirds of the pathway, respectively. Assuming linear motion, the centres of mass in the reconstructed images should be at 1.5 mT and 4.5 mT, which is one and three quarters of the pathway.

Similar results are obtained when emulating motion to 12 mT in x-direction. Using $\mathbf{S}$, the phantom position is estimated at 5 mT, whereas using $\mathbf{S_1}$ and $\mathbf{S_2}$, it is 4.4 mT and 7.4 mT, respectively (values assuming linear motion: 3 mT and 9 mT).

With increasing emulated motion in x-direction, the estimated position in both y- and z-direction moves from the centre of the FOV. As motion has only been emulated in x-direction, the centre position of the phantom should not change in y- and z-direction. The error is lowest when reconstructing with $\mathbf{S}$.

IV. Discussion

IV.I. 1D excitation

The emulated spatial resolution using 1D excitation has been investigated for one particle sample. Two dots of a hybrid 1D phantom could mostly be resolved having a distance of only 0.6 mT to each other. This magnetic field distance corresponds to a spatial distance of 240 µm assuming a magnetic field gradient of 2.5 T m^{-1} in an MPI scanning device. Assuming an even higher magnetic field gradient of 5 T m^{-1} [22], a spatial resolution of 120 µm could be reached.

10.18416/ijmpi.2020.2003004

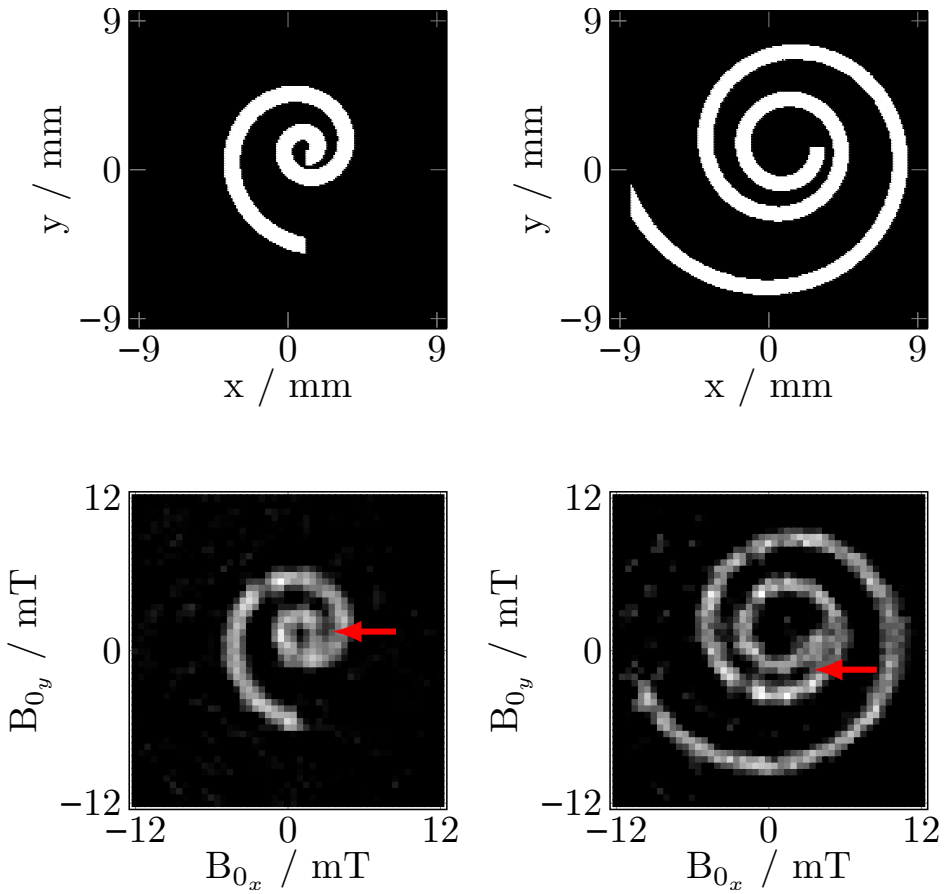

Figure 7: Simulated and reconstructed spiral phantoms. The spiral phantoms presented in [14] featuring channel diameters of 2 mm (left) and 1 mm (right) have been simulated on a fine grid (top). The spatial grid has been converted into a magnetic field grid assuming a gradient field strength of 1.25 T m^{-1}. The discrete points of the spiral phantoms have been subsampled and measured in a multi-dimensional MPS. The received voltage signals have been accumulated. The emulated hybrid phantoms have been reconstructed using a hybrid system matrix (bottom). Both the phantoms are very well represented by the reconstructed images. The curls of the phantoms can be resolved up to a distance of about 1 mT (indicated by the red arrows) corresponding to a spatial resolution of 800 µm.

Currently, a comparable spatial resolution could not be shown using an MPI scanning device. A spatial resolution of MPI in sub-millimetre range has been claimed [3]. This work confirms, that a spatial resolution of few hundred micrometres can be reached using MPI technology. This result could be achieved using the superior SNR of an MPS. The SNR of an MPI scanning device can be increased using dedicated receive coils [23, 24], which may allow for sub-millimetre resolution.

Usually, the receive signals that have been acquired parallel to an excitation direction are being used for system matrix-based reconstruction. Here, it has been confirmed that the reconstructed images benefit from including additional receive channels [12]. The overall SNR of the reconstructed images has increased and the phantoms could be separated more reliably, thus a higher spatial resolution could be achieved. Furthermore, the reconstruction algorithm showed to be more robust.

It has been demonstrated, that a spatial resolution of 240 µm is possible using a magnetic field gradient of 2.5 T m^{-1} in MPI. A 1D excitation field and a single particle sample have been used. The effect of different particle samples, excitation field amplitudes, and frequencies on the SNR and thus, the spatial resolution, should be investigated.

IV.II. 2D excitation

A 2D resolution phantom has been emulated in a multi-dimensional MPS and has been reconstructed using a hybrid system matrix. The point cloud grid with a distance of 1.5 mT could be resolved well, which corresponds to a spatial resolution of 1.2 mm and 600 µm assuming a magnetic field gradient of 1.25 T m^{-1} and 2.5 T m^{-1}, respectively.

The smallest point cloud grid could only be resolved when emulating it on its own. Then, a magnetic field

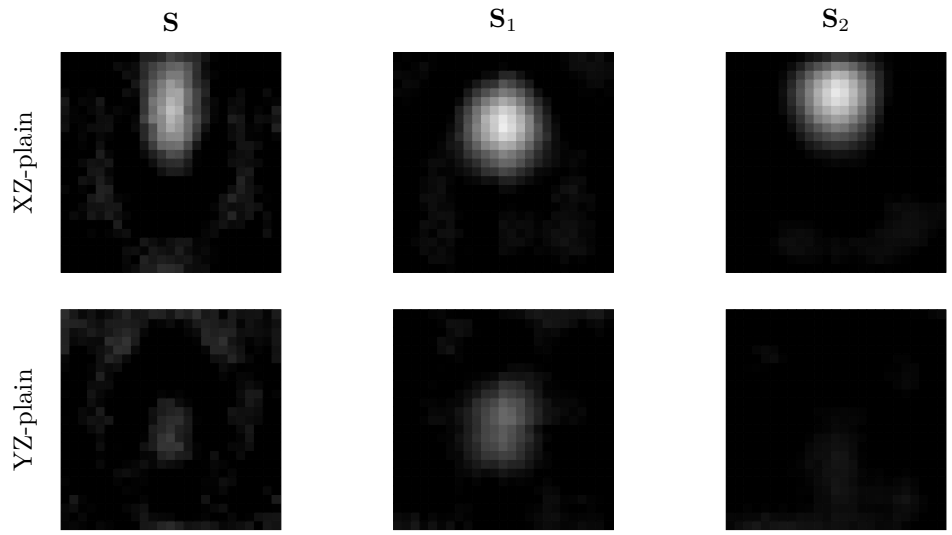

Figure 8: Reconstructed images of an emulated dynamic phantom. Within one drive field cycle, the movement of the phantom from the centre to the border of the FOV in x-direction is emulated using an offset field ramp from 0 mT to 12 mT. The zero plains of xz (top) and yz (bottom) are shown. When reconstructing with the system matrix for the full drive field cycle **S**, the particle sample is reconstructed as a streak from the centre to the border of the FOV in x-direction (top left). The phantom can be identified weakly in the yz-plain (centre position in x-direction, bottom left). After the system matrix and measurement have been split into the two halves of the drive field cycle $\mathbf{S}_1$ and $\mathbf{S}_2$, two different image reconstruction results are obtained. First, the phantom is being reconstructed to the second upper quarter of the xz-plain (top centre). The phantom can still be identified in the corresponding yz-plain (bottom centre). Then, for the second half of the drive field cycle $\mathbf{S}_2$, the phantom is being reconstructed near the border of the FOV (top right). It is not visible in the yz-plain (bottom right).

resolution of 1 mT has been reached corresponding to a spatial resolution of 800 µm and 400 µm, respectively. In the presence of larger point clouds, the smallest point clouds smeared. One reason may be that the signals of small structures are suppressed by the signals of large structures during reconstruction. As 5 % of the points of each simulated point cloud have been selected for emulation, the single point clouds feature a constant particle concentration. However, the signals of the smallest point clouds have been suppressed in the reconstruction result of the whole phantom.

The reconstructed images in Figure 6 show, that a higher spatial resolution can be achieved using a sine-based Lissajous trajectory. Both the measurement parameters and the reconstruction parameters have been the same for the sine- and cosine-based measurement. Due to the higher sampling density of the sine-based Lissajous trajectory, small structures can be resolved better.

The point cloud grid featuring a distance of 1 mT is resolved better along the x-direction (top to bottom). This may be explained by the higher SNR of the receive coil in x-direction. It features the closest distance to the tracer sample and therefore, profits from high signal induction [21].

The reconstructed point clouds near the edges of the FOV are smeared or even missing. It has been described in [4], that the Lissajous trajectory reverses at the edges of the FOV resulting in a low signal induction. Therefore, a low SNR of the measured point clouds can be expected leading to reconstruction artefacts.

Spiral phantoms have been measured in MPI scanning devices for comparative measurements [14]. Here, the spiral phantoms have been simulated in 2D and emulated in a multidimensional MPS. The reconstructed images match the simulated spiral phantoms well. A magnetic field resolution of about 1 mT has been obtained.

IV.III. Dynamic phantoms

Motion has been emulated to a hybrid phantom by a dynamic magnetic offset field. Thus, a dynamic hybrid phantom has been generated. The applied motion has been identified in the reconstructed images as motion artefacts (see Figure 8).

The motion artefacts have been reduced successfully by dedicated reconstructions with system matrices representing the first and second half of the drive field cycle, respectively. Due to the higher frame rate, a better approximation of the particle movement is possible. However, continuous motion will still cause blurring in the reconstructed images, if the displacement within half a drive field cycle is larger than the spatial resolution.

The calculation of the centres of mass reveals a nonlinear emulated motion within the full drive field cycle. As the applied magnetic offset field ramp has not been measured, its linearity can only be assumed. However,

the two experiments introducing motion of 6 mT and 12 mT show similar results in terms of reconstructed motion represented by the centres of mass.

Using 3D excitation, a period of the drive field of 21.54 ms is common, which results in a possible frame rate of 46 Hz. Assuming a spatial resolution of about 1 mm in a current MPI scanning device, biological processes may be monitored that have a velocity of about $0.025\,\mathrm{m\,s^{-1}}$ in terms of single voxel movement following the Nyquist sampling theorem. Thus, the blood flow in human veins and arteries featuring a velocity of about $0.05\,\mathrm{m\,s^{-1}}$ could not be monitored [25]. Here, the temporal resolution of an MPI measurement has been increased by the factor two, which might enable monitoring the blood flow.

V. Conclusion

A valuable tool for investigating field sequences, particles and reconstruction techniques in MPI has been presented. The spatial resolution in MPI for 1D and 2D excitation has been investigated. It has been shown, that MPI technology is capable of reaching a spatial resolution of few hundred micrometers.

It has been demonstrated, that reconstructed images benefit when including additional receive channels into the image reconstruction process in terms of SNR and spatial resolution. Furthermore, a higher spatial resolution was obtained for a sine-based Lissajous trajectory in comparison to a cosine-based one.

Design challenges such as a phantom featuring solid dividing walls with a width in micrometre range can be avoided using hybrid phantoms. The discrete points of a hybrid phantom are emulated by adjusting magnetic offset fields in an MPS. Inaccuracies of the magnetic offset fields may be neglected as they correspond to inaccuracies of few micrometres in spatial domain. As the whole measurement chamber of an MPS emulates an infinitesimal volume inside an MPI scanning device, a large particle sample can be used. However, the particle volume needed will still be limited to tens of micro-litres which is small in comparison to the particle volume of a measurement phantom in an MPI scanning device.

Varying the sampling density of a hybrid phantom, distinct particle concentrations can be emulated. A smeared bolus in a vessel phantom featuring a lot of measurement points in its centre and less at its edges may be emulated.

Furthermore, hybrid phantoms are not limited to static measurements. Dynamic magnetic offset fields emulate a moving phantom. The possibility of generating a dynamic hybrid phantom with distinct particle concentrations and an arbitrary design may facilitate and accelerate MPI research. As the complexity of a hybrid phantom is not limited by construction, accurate animal models may be generated and measured with the hybrid approach, which can help to decrease the number of sacrificed animals.

Hybrid phantoms are a valuable tool for researching the principles of MPI and investigating its limitations. Simulation results can be validated using hybrid phantoms. The signals of different particle types can be compared in reconstructed images guaranteeing a high SNR. Varying the number of receive signal averages, the SNR of the measurements can be increased and the resolution limit may be decreased further.

Blocked particles cannot rotate freely and therefore, may not respond to an excitation direction leading to a low particle signal. It has been suggested in [26] to apply different field sequences sequentially for maximising the particle signal from blocked particles. Applying different field sequences may also increase the spatial resolution in reconstructed images [27]. As multi-dimensional MPS usually support multiple field sequences, hybrid phantoms may be suited for investigating this issue.

Using hybrid phantoms and hybrid system matrices allows for a measurement-based research of field sequences, particles and image reconstruction techniques featuring a very high SNR. The experiments are independent of MPI scanning device reducing the experiment set-up and minimising error sources. MPI research using hybrid phantoms provides a best case scenario in terms of SNR. Therefore, reconstruction results achieved using hybrid phantoms may not be reached in an MPI scanning device. Nevertheless, MPI scanning devices may profit from hybrid phantom research leading to e.g. optimised field sequences. Hybrid phantoms are a valuable instrument for validating the potential of MPI.

Acknowledgments

The authors thankfully acknowledge the financial support by the Federal Ministry of Education and Research (BMBF, grant numbers 13GW0069A and 13GW0230B).

References

[1] M. Graeser, A. von Gladiss, M. Weber, and T. M. Buzug. Two dimensional magnetic particle spectrometry. *Physics in Medicine and Biology*, 62(9):3378–3391, 2017, doi:10.1088/1361-6560/aa5bcd.

[2] A. von Gladiss, M. Graeser, P. Szwargulski, T. Knopp, and T. M. Buzug. Hybrid system calibration for multidimensional magnetic particle imaging. *Physics in Medicine and Biology*, 62(9):3392–3406, 2017, doi:10.1088/1361-6560/aa5340.

[3] T. Knopp, S. Biederer, T. F. Sattel, M. Erbe, and T. M. Buzug. Prediction of the spatial resolution of magnetic particle imaging using the modulation transfer function of the imaging process. *IEEE Transactions on Medical Imaging*, 30(6):1284–1292, 2011, doi:10.1109/TMI.2011.2113188.

[4] T. Knopp, S. Biederer, T. F. Sattel, J. Weizenecker, B. Gleich, J. Borgert, and T. M. Buzug. Trajectory analysis for magnetic particle imaging. *Physics in Medicine and Biology*, 54(2):385–397, 2009, doi:10.1088/0031-9155/54/2/014.

[5] M. Graeser, K. Bente, A. Neumann, and T. M. Buzug. Trajectory dependent particle response for anisotropic mono domain particles in magnetic particle imaging. *Journal of Physics D: Applied Physics*, 49(4):045007, 2016, doi:10.1088/0022-3727/49/4/045007.

[6] B. Gleich and J. Weizenecker. Tomographic imaging using the nonlinear response of magnetic particles. *Nature*, 435(7046):1214–1217, 2005, doi:10.1038/nature03808.

[7] L. R. Croft, P. W. Goodwill, and S. M. Conolly. Relaxation in X-Space Magnetic Particle Imaging. *IEEE Transactions on Medical Imaging*, 31(12):2335–2342, 2012, doi:10.1109/TMI.2012.2217979.

[8] P. W. Goodwill and S. M. Conolly. The X-Space Formulation of the Magnetic Particle Imaging Process: 1-D Signal, Resolution, Bandwidth, SNR, SAR, and Magnetostimulation. *IEEE Transactions on Medical Imaging*, 29(11):1851–1859, 2010, doi:10.1109/TMI.2010.2052284.

[9] D. Schmidt, M. Graeser, A. von Gladiss, T. M. Buzug, and U. Steinhoff. Imaging Characterization of MPI Tracers Employing Offset Measurements in a two Dimensional Magnetic Particle Spectrometer. *International Journal on Magnetic Particle Imaging*, 1(2), 2016, doi:10.18416/IJMPI.2016.1604002.

[10] C. Debbeler, A. von Gladiss, T. Friedrich, T. M. Buzug, and K. Lüdtke-Buzug, New MPI Tracer Material - A Resolution Study, in *International Workshop on Magnetic Particle Imaging*, 33–34, 2018.

[11] A. von Gladiss, M. Graeser, and T. M. Buzug, Influence of Excitation Signal Coupling on Reconstructed Images in Magnetic Particle Imaging, in *Bildverarbeitung für die Medizin 2018. Informatik aktuell*, Springer Vieweg, 2018, 92–97. doi:10.1007/978-3-662-56537-7_36.

[12] M. Graeser, F. Thieben, P. Szwargulski, F. Werner, N. Gdaniec, M. Boberg, F. Griese, M. Möddel, P. Ludewig, D. van de Ven, O. M. Weber, O. Woywode, B. Gleich, and T. Knopp. Human-sized magnetic particle imaging for brain applications. *Nature Communications*, 10(1):1936, 2019, doi:10.1038/s41467-019-09704-x.

[13] S. Biederer, T. F. Sattel, T. Knopp, and T. M. Buzug, Variable Trajektoriendichte für Magnetic Particle Imaging, in *Bildverarbeitung für die Medizin 2010*, 2010.

[14] O. Kosch, H. Paysen, J. Wells, F. Ptach, J. Franke, L. Wöckel, S. Dutz, and F. Wiekhorst. Evaluation of a separate-receive coil by magnetic particle imaging of a solid phantom. *Journal of Magnetism and Magnetic Materials*, 471:444–449, 2019, doi:10.1016/j.jmmm.2018.09.114.

[15] J. Weizenecker, B. Gleich, J. Rahmer, H. Dahnke, and J. Borgert. Three-dimensional real-time in vivo magnetic particle imaging. *Physics in Medicine and Biology*, 54(5):L1–L10, 2009, doi:10.1088/0031-9155/54/5/L01.

[16] B. Zheng, T. Vazin, P. W. Goodwill, A. Conway, A. Verma, E. Ulku Saritas, D. Schaffer, and S. M. Conolly. Magnetic Particle Imaging tracks the long-term fate of in vivo neural cell implants with high image contrast. *Scientific Reports*, 5(1):14055, 2015, doi:10.1038/srep14055.

[17] N. Gdaniec, P. Szwargulski, M. Möddel, M. Boberg, and T. Knopp, Multi–patch magnetic particle imaging of a phantom with periodic motion, in *International Workshop on Magnetic Particle Imaging*, 27–28, 2019.

[18] M. N. Schauerte, P. Szwargulski, M. G. Kaul, T. Knopp, and M. Graeser, A Schematic Kidney Phantom for Magnetic Particle Imaging, in *International Workshop on Magnetic Particle Imaging*, 59–60, 2019.

[19] P. Szwargulski, M. Exner, P. Ludewig, T. Knopp, and M. Graeser, From a static to a dynamic 3D anatomical phantom of a rat, in *Additive Manufacturing Meets Medicine 1 (S1)*, 2019.

[20] A. von Gladiss, M. Graeser, and T. M. Buzug, Increasing the MPI Frame Rate by Excitation Signal Phase-Shifting and Receive-Signal-Splitting, in *International Workshop on Magnetic Particle Imaging*, 215–216, 2018.

[21] X. Chen, M. Graeser, A. Behrends, A. von Gladiss, and T. M. Buzug. First Measurement Results of a 3D Magnetic Particle Spectrometer. *International Journal on Magnetic Particle Imaging*, 4(1), 2018, doi:10.18416/IJMPI.2018.1810001.

[22] M. Weber, J. Beuke, A. von Gladiss, K. Gräfe, P. Vogel, V. C. Behr, and T. M. Buzug. Novel Field Geometry Using Two Halbach Cylinders for FFL-MPI. *International Journal on Magnetic Particle Imaging*, 4(2), 2018, doi:10.18416/IJMPI.2018.1811004.

[23] M. Graeser, T. Knopp, P. Szwargulski, T. Friedrich, A. von Gladiss, M. Kaul, K. M. Krishnan, H. Ittrich, G. Adam, and T. M. Buzug. Towards Picogram Detection of Superparamagnetic Iron-Oxide Particles Using a Gradiometric Receive Coil. *Scientific Reports*, 7(1):6872, 2017, doi:10.1038/s41598-017-06992-5.

[24] H. Paysen, J. Wells, O. Kosch, U. Steinhoff, J. Franke, L. Trahms, T. Schaeffter, and F. Wiekhorst. Improved sensitivity and limit-of-detection using a receive-only coil in magnetic particle imaging. *Physics in Medicine & Biology*, 63(13):13NT02, 2018, doi:10.1088/1361-6560/aacb87.

[25] M. Klarhöfer, B. Csapo, C. Balassy, J. Szeles, and E. Moser. High-resolution blood flow velocity measurements in the human finger. *Magnetic Resonance in Medicine*, 45(4):716–719, 2001, doi:10.1002/mrm.1096.

[26] A. von Gladiss, M. Graeser, K. Lüdtke-Buzug, and T. M. Buzug. Contribution of brownian rotation and particle assembly polarisation to the particle response in magnetic particle spectrometry. *Current Directions in Biomedical Engineering*, 1(1):298–301, 2015, doi:10.1515/cdbme-2015-0074.

[27] F. Werner, N. Gdaniec, and T. Knopp. Improving the Spatial Resolution of Bidirectional Cartesian MPI Data using Fourier Techniques. *International Journal on Magnetic Particle Imaging*, 3(1), 2017, doi:10.18416/IJMPI.2017.1703007.

